PNAS RESEARCH ARTICLE | ENGINEERING

Loss-free tensile ductility of dual-structure titanium composites via an interdiffusion and self-organization strategy

Lei Liu[a], Shufeng Li[a,b,1], Deng Pan[a,c], Dongxu Hui[a], Xin Zhang[a,b], Bo Li[a,b], Tianshou Liang[d], Pengpeng Shi[d,e,1], Abdollah Bahador[f,g], Junko Umeda[f], Katsuyoshi Kondoh[f], Shaolong Li[a], Lina Gao[a], Zhimao Wang[h], Gang Li[h], Shuyan Zhang[i], Ruihong Wang[a,b], and Wenge Chen[a,b]

Edited by Alexis Bell, University of California, Berkeley, CA; received February 8, 2023; accepted May 15, 2023

The deformation-coordination ability between ductile metal and brittle dispersive ceramic particles is poor, which means that an improvement in strength will inevitably sacrifice ductility in dispersion-strengthened metallic materials. Here, we present an inspired strategy for developing dual-structure-based titanium matrix composites (TMCs) that achieve 12.0% elongation comparable to the matrix Ti6Al4V alloys and enhanced strength compared to homostructure composites. The proposed dual-structure comprises a primary structure, namely, a TiB whisker-rich region engendered fine grain Ti6Al4V matrix with a three-dimensional micropellet architecture (3D-MPA), and an overall structure consisting of evenly distributed 3D-MPA "reinforcements" and a TiBw-lean titanium matrix. The dual structure presents a spatially heterogeneous grain distribution with 5.8 μm fine grains and 42.3 μm coarse grains, which exhibits excellent hetero-deformation-induced (HDI) hardening and achieves a 5.8% ductility. Interestingly, the 3D-MPA "reinforcements" show 11.1% isotropic deformability and 66% dislocation storage, which endows the TMCs with good strength and loss-free ductility. Our enlightening method uses an interdiffusion and self-organization strategy based on powder metallurgy to enable metal matrix composites with the heterostructure of the matrix and the configuration of reinforcement to address the strength-ductility trade-off dilemma.

titanium matrix composites (TMCs) | dual structure | interdiffusion | hetero-deformation-induced (HDI) hardening | powder metallurgy

Significance

High strength-ductility pursuit in metallic materials has been a long endeavor for advanced engineering applications. However, the accumulation and entanglement of massive dislocations in dispersion-strengthened metal matrix composites (MMCs) produce local stress concentrations, causing serious strength-ductility trade-off which impede its extensive applications. Herein, we developed a structure control method named interdiffusion and self-organization strategy based on powder metallurgy for preparing dual-structure Ti6Al4V-TiBw composites with matrix heterostructure and reinforcement configuration design, achieving a high strength-ductility synergy which practically unattainable in homogeneous MMCs. Our strategy sheds light on the development of high-performance MMCs, which are excepted to be applied to other metallic materials and MMCs to promote lightweight engineering.

Pursuing high strength and high ductility in metallic materials has been a lasting endeavor for advanced engineering applications (1–3). Increasing the yield strength of metals utilizing dispersive second-phase particles that impede dislocation motion is one of the most common strengthening methods. These concepts have been widely used in the room-/high-temperature strengthening of titanium, aluminum, magnesium, and copper alloys and other metallic materials (4–8). It has been generally recognized that the strengthening effect is usually dominated by the interaction between dislocations and the elastic strain energy generated by second-phase particles (9). However, the deformation mismatch due to the significant difference in physical properties between second-phase particles and the metal matrix is the leading cause of massive dislocation accumulation and entanglement which result in local stress concentrations (10). The exacerbation of the strain localization degree near the interface between second-phase particles and the metal matrix promotes crack initiation and extension, which seriously deteriorates ductility and toughness (11–13).

Introducing low-energy phase interfaces and/or eliminating the intergranular distribution of second-phase particles are currently the main strategies for relieving local stress concentrations in dispersion-strengthened metallic materials (5, 9, 14–17). The former strategy usually involves alloying designs to obtain a low-energy phase interface, reducing the difference in mechanical properties between the two phases and thereby relieving local stress concentrations to overcome the strength-ductility trade-off dilemma (5, 9, 14, 15). In another strategy, strengthening is achieved by reducing the grain boundary aggregation of second-phase particles to relieve the local stress concentration of metallic materials (16, 17). The above strategies have recently been demonstrated in both second-phase dispersion-strengthened maraging steels (5, 9) and oxide dispersion-strengthened metallic materials (17). Both distinct tactics share a unifying character in that the second-phase particles are distributed dispersedly, which leads to an overhardened metal matrix state due to a drastic reduction in the mean free paths of dislocation motion (18). This feature is dramatically amplified in developing metal matrix composites (MMCs) based on dispersion-strengthened metallic materials (19). Such a destructive distribution behavior of second-phase particles in MMCs incredibly leads to unpredictable fracture failure and inhibits the full exploitation of the "1 + 1 > 2" performance advantage by utilizing the ductility of metals and the hardness of second-phase particles.

Author contributions: L.L., Shufeng Li, D.H., X.Z., and B.L. designed research; L.L., D.H., and Shaolong Li performed research; Shufeng Li, T.L., P.S., A.B., J.U., K.K., Z.W., G.L., and S.Z. contributed new reagents/analytic tools; L.L., Shufeng Li, D.P., D.H., X.Z., B.L., T.L., P.S., A.B., K.K., Shaolong Li, L.G., Z.W., G.L., R.W., and W.C. analyzed data; and L.L., Shufeng Li, D.P., X.Z., B.L., T.L., P.S., and L.G. wrote the paper.

The authors declare no competing interest.

This article is a PNAS Direct Submission.

[1]To whom correspondence may be addressed. Email: shufengli@xaut.edu.cn or shipengpeng@xjtu.edu.cn.

This article contains supporting information online at https://www.pnas.org/lookup/suppl/doi:10.1073/pnas.2302234120/-/DCSupplemental.

Published July 3, 2023.

Inspired by natural structures, the configuration design concept using the microstructure as a design factor has become a fundamental way to break the strength-ductility trade-off dilemma of MMCs (20, 21). A series of typical configuration design strategies for MMCs have been proposed by tailoring the reinforcement spatial distribution (TRSD) (21–25), such as "network," "laminated," "multicore," "gradient," "brick-mortar," and "bi/multimodal" structures. These strategies mostly employ introducing a plastic deformation zone around the second-phase particles to blunt the crack tip and buffer crack propagation to reduce the overhardened state of MMCs and enhance their fracture elongation. In titanium, aluminum, and copper matrix composites with a network structure, for instance, a large number of intergranular reinforcements such as TiB whisker (TiBw), Al_2O_3, and graphene can in situ form three-dimensional (3D) discontinuous networks to achieve dislocation storage and induce crack bridging, in which the modulus, strength, plasticity, and toughness of the composites can be simultaneously enhanced (22, 26, 27). Despite the above progress, these design concepts are characterized by a single configuration of the interface. This is not conducive to the pinning and storage of dislocations, thus leading to insufficient strain hardening of the matrix in the single-configuration MMCs. Consequently, optimizing the interface between the matrix and reinforcements is crucial for alleviating local stress concentration and achieving strength-ductility synergy for MMCs.

Heterostructure materials provide perspectives by activating hetero-deformation-induced (HDI) hardening effectiveness to improve the mechanical properties of metallic materials. As suggested by the strain-gradient plasticity theory in micromechanics (28), incompatible deformation of two phases generates a strain gradient near the interface, and the greater the difference in mechanical properties is, the more significant the strain gradient should be. This leads to a pileup of geometrically necessary dislocations (GNDs) near the interface and induces the formation of back stresses in the soft regions (coarse-grained region) and forward stresses in the hard regions (fine-grained region), which jointly produce the so-called HDI hardening that enhances strain hardening resulting in the retention of ductility (29). In this way, the strain hardening effectiveness of MMCs can be compensated by designing heterogeneous grain structures (25). However, current approaches fabricating MMCs have difficulties in controlling grain size. A remarkable strength-ductility enhancement is expected if we could construct a microscopic gradient structure with a multi-interface by introducing a fine-grained region between the coarse-grained region and reinforcement via structural design. This will provide alternative design strategies to address the challenge of insufficient strain hardening for single-configuration MMCs.

Inspired by the above idea, we have developed an interdiffusion and self-organization strategy for preparing dual-structure Ti6Al4V-TiBw composites (as shown in Fig. 1*A*) that achieves a good match between high strength and high ductility. This strategy constructs a special configuration of reinforcements and heterogeneous grain structures of the matrix by utilizing the interdiffusion reaction mechanism between alloying elements and the matrix in titanium matrix composites (TMCs). These Ti6Al4V-TiBw composites exhibit a dual structure, i.e., TiBw-rich regions named the "primary" structure with a three-dimensional micropellet architecture (3D-MPA) and a composite structure comprised of 3D-MPA as the "reinforcements" and TiBw-lean regions named the "overall" structure. The introduction of a multi-interface endows the 3D-MPA "reinforcements" with dislocation storage ability and isotropic deformability, alleviating the local stress concentration problem caused by deformation mismatch in single-configuration MMCs. On the other hand, the heterogeneous grain structures produce additional HDI strengthening/hardening effects for the Ti6Al4V-TiBw composites. Therefore, this dual-structure Ti6Al4V-TiBw composite obtains an excellent elongation that is comparable to the Ti6Al4V alloy while improving the strength, effectively overcoming the strength-ductility trade-off in TMCs. Our strategy paves a thrilling way for developing high-performance MMCs with good strength-ductility compatibility, which can be applied to other metallic materials and MMCs to promote lightweight engineering to help address the current challenge of the energy crisis and global warming.

Results and Discussion

Microstructural Characterization. The scanning electron microscopy (SEM) imaging and synchrotron radiation imaging results reveal a hierarchical structure of the dual-structure Ti6Al4V-TiBw composites (Fig. 1*A*), i.e., the primary structure and the overall structure. Fig. 1*B* shows EBSD image quality mapping of dual structure. During the sintering process of the powder mixture, containing a spherical Ti-TiBw composite powder, Al powder, and vanadium (V) powder, an interdiffusion reaction occurs between Ti and Al, V elements. This reaction leads to the formation of TiBw-rich region within the Ti-TiBw composite powder, resulting in the 3D-MPA known as primary structure. This process results in a 10 vol.% content of TiBw inside the 3D-MPA of the dual-structure composites, which is significantly higher than 3.4 vol.% content of TiBw in spherical Ti-TiBw composite powder. *SI Appendix*, Figs. S1 and S2 provides additional detailed characteristics of the TiBw features in the Ti-TiBw composites powder and the dual-structure Ti6Al4V-TiBw composites. Furthermore, the Ti6Al4V matrix in the 3D-MPA forms fine grains due to the pinning effect of TiBw. For the overall structure, TiBw colonies with a 3D-MPA shape are evenly distributed in the Ti6Al4V matrix (Fig. 1*A* and Movies S1 and S2), and coarse grains appear in the area except that occupied by the 3D-MPA (Fig. 1*B*), which forms 3D-MPA reinforced Ti6Al4V matrix composites at the macroscale. Hence, the dual structure has TiBw reinforcements with TRSD architectures and a heterogeneous grain structure composed of fine and coarse grains in the matrix (see Fig. 2*A* for the statistics of the grain size distributions). This dual structure has an important influence on the mechanical behavior of TMCs.

Composite Powder. The spherical Ti-TiBw composite powder established by our previous work (33, 34) is one of the key synthetic strategies to produce this dual structure. Since the traditional high-energy ball milling method is prone to introduce undesired contamination (such as oxygen, nitrogen, and hydrogen) (35, 36), the electrode induction gas atomization (EIGA) method is recommended for preparing the high-purity spherical Ti-TiBw composite powder, further preventing the introduction of impurity elements during the preparation of the dual-structure composites. *SI Appendix*, Fig. S2 exhibits the microstructure characteristics of our as-prepared spherical Ti-TiBw composite powder with 3.4 vol.% TiBw. Ultra-fine networks of nano-TiBw with 20 to 40 nm in width and several hundred nanometers in length are successfully engendered in the Ti matrix (*SI Appendix*, Fig. S2 *B* and *C*) and distributed along grain boundaries (GBs) and formed an ultrafine equiaxed network. Additionally, the spherical Ti-TiBw composite powder is the key to tune the distribution characteristics of the 3D-MPA and the fine-grained region size formed by the Zener pinning effect of TiBw during the sintering process.

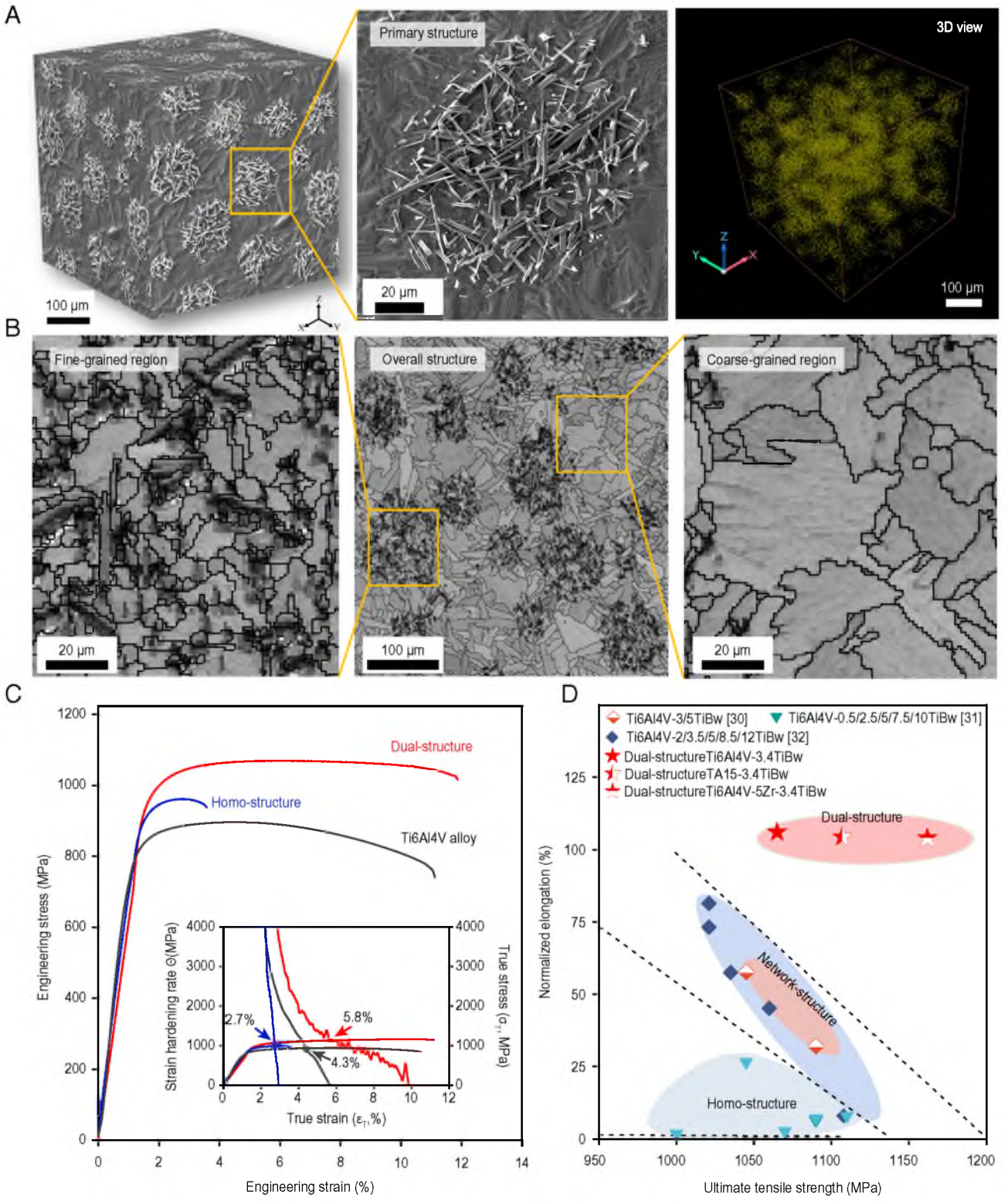

Fig. 1. Typical microstructural and mechanical properties of dual-structure Ti6Al4V-TiBw composites. (*A*) Hierarchical arrangements of 3D-MPA "reinforcement" in the Ti6Al4V matrix. (*B*) The image quality mapping of dual-structure Ti6Al4V-TiBw composites in electron backscatter diffraction (EBSD), wherein rectangle marks showing the fine- and coarse-grained region. (*C*) Representative engineering stress–strain curves for dual structure and homo structure, as well as Ti6Al4V alloy. The inset shows the corresponding true stress–strain curves and hardening rate–true strain curves. (*D*) The Ashby plot of normalized elongation vs. ultimate tensile strength in this work and refs. 30–32.

Mechanical Properties. The dual-structure composite achieves remarkable improvement in tensile properties. We observed a significant enhancement in ductility, quantified from engineering stress–strain curves (Fig. 1*C*), of the dual-structure Ti6Al4V-TiBw composites compared to the homostructure counterparts (uniformly distribution of TiBw reinforcements). The fracture elongation tripled, increasing from 3.6 ± 0.31% for the homostructure to 12.0 ± 0.48% for the dual structure,

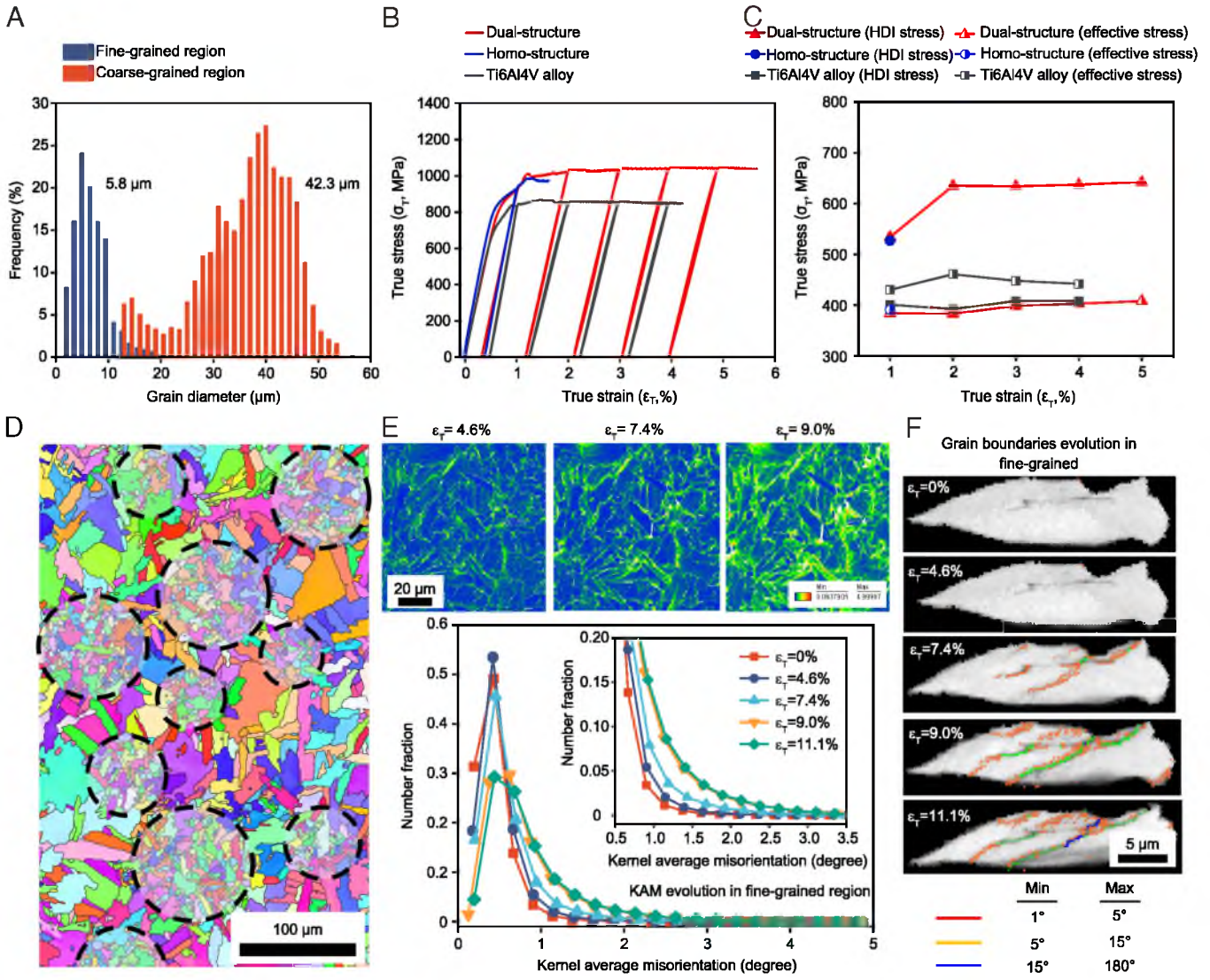

Fig. 2. HDI hardening of dual-structure Ti6Al4V-TiBw composites. (*A*) EBSD statistical data of grain size in the fine- and coarse-grained regions. (*B*) loading–unloading–reloading (LUR) stress–strain curves comparison of dual-structure, homostructure Ti6Al4V-TiBw composites and Ti6Al4V alloys. (*C*) The strength contribution of HDI stress and effective stress for dual-structure Ti6Al4V-TiBw composites. (*D*) inverse pole figure (IPF) mapping in dual-structure Ti6Al4V-TiBw composites, where the area selected by the dashed circles indicates the fine-grained region. (*E*) The distribution of kernel average misorientation (KAM) in the fine-grained region and its KAM values at plastic strain of 0%, 4.6%, 7.4%, 9.0%, and 11.1%. (*F*) The transition of high- to low-angle grain boundary of the fine grain inside primary structure.

and was comparable to that of the widely studied Ti6Al4V alloy of 10.9 ± 0.68% in this study and 11.3 ± 1.1% in ref. 30. Additionally, we measured yield strength (YS) and ultimate tensile strength (UTS) up to 1,023 ± 17 MPa and 1,065 ± 25 MPa, respectively, for dual-structure samples, physically increased compared to that of homostructure (950 ± 30 MPa for YS and 961 ± 34 MPa for UTS, respectively). *SI Appendix*, Table S1 lists several different spatial distribution characteristics of the TiBw in TMCs and their effectiveness in improving strength and ductility for comparation. The detailed mechanism of our present dual structure is discussed in the following subsection. Moreover, the fracture energy, calculated by the integral area underneath the true stress–strain curve, is also provided to gain additional insight into the toughening effect. The fracture energy of the dual structure is 116 ± 7 J m^{-3}, which is approximately four times higher than that of the homostructure (28 ± 13 J m^{-3}). This implies that this unique dual structure leads to a significant toughening effect. The detailed mechanical properties are listed in *SI Appendix*, Table S2.

We also plotted the strain hardening rate Θ ($\Theta = d\sigma_T / d\varepsilon_T$, where σ_T is the true stress and ε_T is the true strain) vs. true strain curves to understand the deformation behaviors at the macroscopic level (see the *Inset* in Fig. 1*C*). The dual structure exhibits a steady strain hardening behavior (with a 5.8% ductility), i.e., Θ sustainably decreases after yielding and then enters a stable strain-softening stage until reaching the tensile plastic instability criterion (8). In comparison, the Θ value of the homostructure drops rapidly before meeting the instability criterion. It follows that the dual structure exhibits a higher Θ (see the *Inset* in Fig. 1*A*), enabling unexpected drastic increase in ductility. Combing the resulting strength ductility and especially the fracture elongation of the dual-structure Ti6Al4V-TiBw composites outperforms that of any other architecture TMCs in unformed state (30–32) (Fig. 1*D*). We also fabricated similar dual structures in other TMC systems, such as Ti-6.5Al-2Zr-1Mo-1V-TiBw and Ti6Al4V-5Zr-TiBw (as shown in *SI Appendix*, Table S3), in which excellent strength-ductility synergy was obtained, implying that this dual structure is well adaptive in other TMCs.

Hetero-Deformation-Induced Hardening. We attributed the pronounced increase in the strain hardening rate Θ to the HDI hardening effect originated from heterogeneous grain structure. The grain information of the dual-structure composites was analyzed by using EBSD. As revealed by the IPF mapping in Fig. 2*D*, the average grain size of the matrix within the 3D-MPA area is approximately 5.8 μm, while 42.3 μm for the matrix outside of the 3D-MPA, indicating a distinct fine- and coarse-grained region (Fig. 2*A*). It follows that the dual structure divides the composite into soft and hard regions (Fig. 2*D*). Near the heterointerface between soft and hard regions, there are dramatic differences in the strength and strain hardening capability (29, 37, 38). Hetero-deformation caused by this mechanical incompatibility can introduce a strain gradient near the interfaces where some GND pileups at the interface; this contributes to the HDI hardening effect providing high strength and ductility for the dual-structure composites. Consequently, optimizing the proportion of coarse and fine grains is crucial to the strength-ductility synergy for the dual-structure Ti6Al4V-TiBw composites, which can be controlled by modulating the contents of alloying elements Al involved in the interdiffusion reaction and the volume fraction of TiBw within the 3D-MPA.

We conducted a LUR experiment (37) to test the Bauschinger effect and evaluate the HDI hardening effect of the dual-structure Ti6Al4V-TiBw composites. Fig. 2*B* shows the typical LUR curves for the dual structure, homostructure composites, and the Ti6Al4V alloy. Both of the dual structure and Ti6Al4V alloy samples exhibit a hysteresis loop of the Bauschinger effect, indicating the existence of inhomogeneous deformation (37). Interestingly, the hysteresis loop of dual-structure composites becomes more significant with increasing strain state compared to the minor differences in the Ti6Al4V alloy. The contributions of the HDI stress to the flow stress from the LUR curves were estimated (Fig. 2*C*). The HDI stress enhances with the increase of plastic strain, especially in the early strain stage, contributing to the onset of high strain hardening, which is the key to the high Θ value of the dual-structure Ti6Al4V-TiBw composites. These features indicate that we could optimize TMCs properties by constructing a heterogeneous fine- and coarse-grained structure.

High GND pileup density is expected to produce HDI hardening (37). Here, we quantitatively analyzed the GND evolution by measuring the local crystal orientation with EBSD by an in situ tensile test. The local misorientation was determined by the KAM method, where the higher KAM values correspond to higher GND densities (39). The obtained KAM maps are shown in Fig. 2*E* and *SI Appendix*, Fig. S3 for fine- and coarse-grained regions of dual-structure composites under corresponding tensile strains. KAM is elevated with increasing tensile strain, indicating an increase trend in the GND density. Since the GND density is related to the strain gradient (28, 39), these results suggest that the strain gradient becomes more severe with increasing tensile strain. The increasing strain gradient contributes to the HDI hardening effect, which enhances the strain hardening ability and ductility (38, 39). Notably, high KAM values are mainly located at the GBs and around the TiBw reinforcements during tensile deformation. These GBs and reinforcements serve as barriers to dislocation motion and, therefore, locally generate GNDs (40, 41). Since thermal mismatch stress-induced dislocations preexist before the plastic deformation, these defects contribute to the enhancement of the yield strength of composites (42), where *SI Appendix*, Supplementary Note 2 discusses the strengthening mechanism of the dual-structure Ti6Al4V-TiBw composites.

Additionally, we observed that some grains transform from low-angle grain boundaries (LAGBs) to high-angle grain boundaries (HAGBs) and then generate additional grains under increasing strain (*SI Appendix*, Fig. S4 and Fig. 2*F*). The increased strain gradient is mainly distributed near the GBs and the subgrain boundaries (SGBs) (Fig. 2*E*). The transformation from LAGBs to HAGBs is primarily related to the entanglement and accumulation of dislocations (43). HAGBs store more dislocations (43), which can provide more spaces for GND pileups. As such, the HDI hardening in the presence of HAGBs becomes much more significant. It is shown that the introduction of the fine-grained region can effectively contribute to the elevation of HDI stresses within the dual-structure Ti6Al4V-TiBw composites. This observation also supports the above assertion regarding HDI hardening.

Dislocation Storage and Deformation Ability of 3D-MPA Reinforcements. We further statistically analyzed the variations of GND densities in the fine- and coarse-grained regions under different strains through the KAM distribution (Fig. 3*A* and *SI Appendix*, Fig. S3). The fine-grained region has a considerable GND density (~66% of the total), showing significant increment with increasing strain. The high-density dislocations suggest that the dual structure endows the 3D-MPA with excellent dislocation storage ability, which gives the TMCs good strength and loss-free ductility. Additional observations by transmission electron microscopy (TEM) show a large number of high-density dislocations located preferentially in the soft phase near the heterointerface and the interface between fine grains and TiBw (Fig. 3*B* and *SI Appendix*, Fig. S5) after tensile deformation. This indicates that the soft phase experienced sufficient plastic deformation before failure. The pileup of dislocations in the soft phase was built to accommodate the pronounced strain gradient stimulated by the heterogeneous deformation between two phases, which produces HDI stress and thus greatly enhances the strain hardening capability of the soft phase (37). We also performed EBSD analysis focused on an individual 3D-MPA with different tensile strains (4.6%, 7.4%, 9.0%, and 11.1%). The IPF mapping shows the evolution of grain orientation in the fine-grained region (Fig. 3*C*). For the grains marked with golden triangles (α-titanium), the grains slipped or rotated with increasing tensile strain, showing a significant plastic deformation behavior. After counting the size changes of the fine grains before and after tensile deformation, the deflection in the fine grains reached ~11.1% before fracture as shown in Fig. 3*E*.

The dislocation configurations of the α-titanium grains in the 3D-MPA "reinforcements" were further investigated to gain insight into the deformation characteristics of the soft phase. A representative fine grain was tilted to particular reflections at the $[\bar{1}2\bar{1}0]$ zone axis to illuminate <a>, <c>, and <c+a> dislocations separately by considering the *HCP* lattice structure for α-titanium. Two-beam conditions with different diffraction vectors were set up during TEM observations (*SI Appendix*, Fig. S6). Based on the invisibility criterion of $\vec{g} \cdot \vec{b} = 0$, where $\vec{g}$ is the diffraction vector and $\vec{b}$ is the Burgers vector, the <a> component is out of contrast when $\vec{g} = (0002)$, whereas the <c> component is out of contrast when $\vec{g} = (10\bar{1}0)$ or $\vec{g} = (10\bar{1}1)$. The dislocations in the fine-grained region can be divided into basal <a> and prismatic <a>, pyramidal <a>, and <c+a> types. Due to the high mismatch stress caused by the surrounding TiBw, the pyramidal <a> and <c+a> dislocations are fully activated. Activation of the multislip system suggests that these constrained fine grains in the 3D-MPA plastically deform at high stresses, giving the 3D-MPA "reinforcements" strong strain hardening and high deformation ability in the dual-structure Ti6Al4V-TiBw composites. This indicates that the dual structure provides the 3D-MPA "reinforcements" an

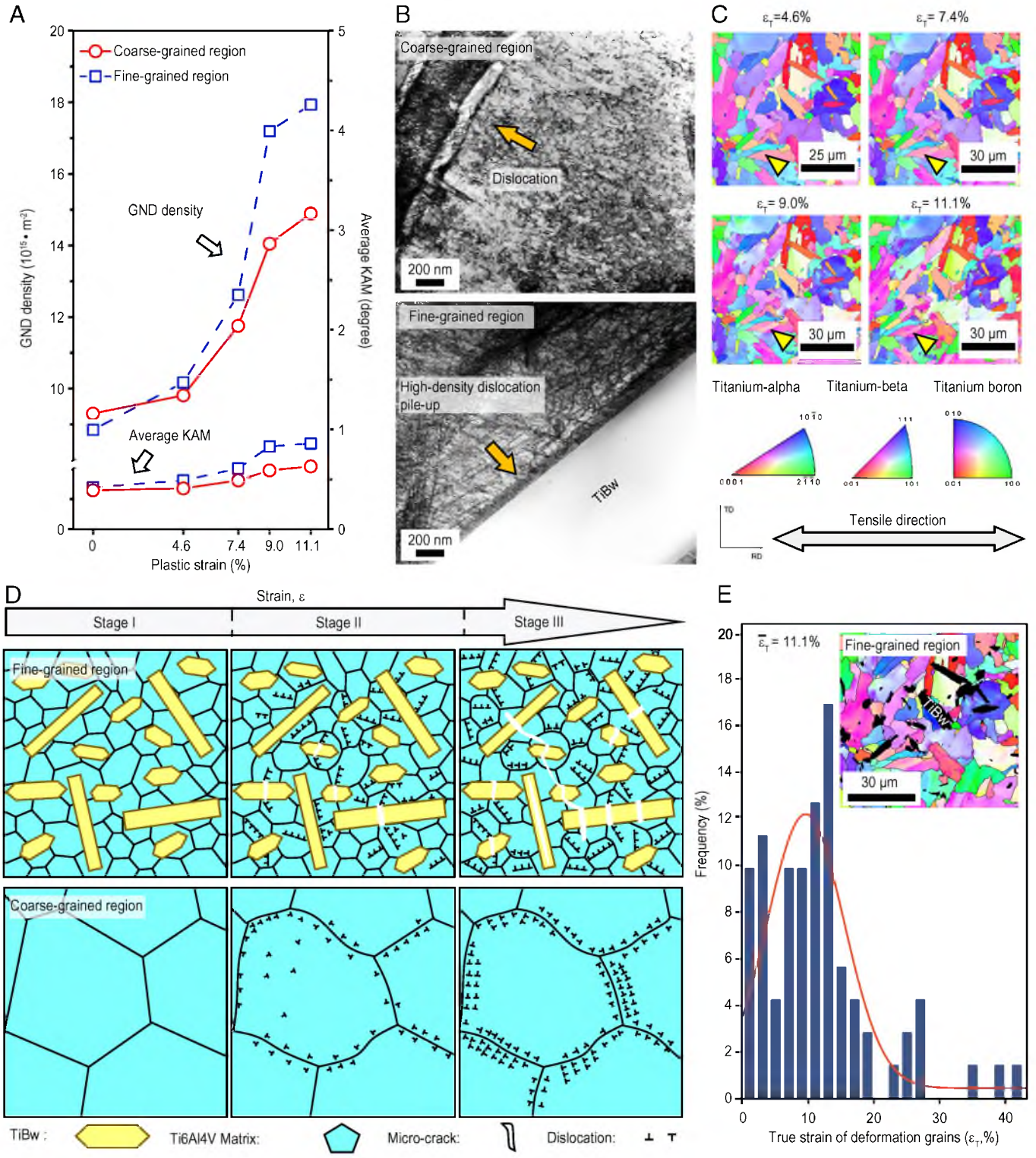

Fig. 3. Dislocation distribution of dual-structure Ti6Al4V-TiBw composites. (*A*) The GND density of dual-structure Ti6Al4V-TiBw composites at different strains. (*B*) Representative TEM images for the dual-structure Ti6Al4V-TiBw composites after tensile testing, where the matrix shows high-density dislocation pileups in the fine-grained region and coarse-grained region. (*C*) IPF mapping of the grain evolution in fine-grained region under different strains of 4.6%, 7.4%, 9.0%, and 11.1%, respectively. (*D*) Schematic illustration of the dislocation behavior during deformation. Stage I: elastic deformation, stage II: elastic–plastic deformation, and stage III: larger plastic deformation. (*E*) Distribution of fine grains strains inside 3D-MPA with an average true strain of 11%.

excellent deformation ability which improve the deformation coordination. Moreover, due to the interplay between the fine- and coarse-grained regions for accommodating the strain incompatibilities, the presence of strain gradients can also induce multiaxial stress developed from the applied uniaxial stress, activating other slip systems and dislocation accumulation (23).

We also present a schematic explanation of the dislocation behaviors in the fine- and coarse-grained regions of the dual-structure Ti6Al4V-TiBw composites (Fig. 3*D*). For the fine-grained region, the dislocation behavior of the 3D-MPA "reinforcements" in different stages was analyzed. In stage I, the TiBw and Ti6Al4V matrix only undergo elastic deformation,

similar to the conventional homostructure TMCs. In stage II, the Ti6Al4V matrix begins to undergo plastic deformation, and the deformation mismatch between the Ti6Al4V matrix and TiBw leads to a strain gradient near the interface. Part of the GNDs accumulated around the TiBw, which broke the TiBw along the axial direction of [010]. The other part of the GNDs is bound in the fine grains, and further entanglement and accumulation occur (Fig. 3*D*). With a further increase in the strain, the composites in stage III approach fracture failure. At this stage, the matrix grains in the 3D-MPA accommodate most of the plastic strain, and deformation-induced dislocation accumulation emerges, even leading to the formation of SGBs. The fine- and coarse-grained regions in the Ti6Al4V matrix are connected in the overall structure. Hence, the coarse grain can effectively relieve the local stress concentrations originating from the fine-grained region. For the coarse-grained region, dislocations gradually accumulate on the grain boundary as strain increase. The deformability and dislocation storage of 3D-MPA "reinforcements" endow the dual-structure composites with good strength and loss-free ductility.

Mechanical Behaviors Controlled by 3D-MPA Spacing. The mechanical properties of fine- and coarse-grained regions in the dual-structure Ti6Al4V-TiBw composites were characterized using the nanoindentation method. The typical indentation load–displacement curves and nanoindentation micrographs for these regions are displayed in Fig. 4 *A* and *B*, respectively. The mechanical properties obtained are summarized in *SI Appendix*, Table S4. These regions in the dual-structure composites show distinct mechanical properties. Owing to the introduction of the fine-grained region which exhibits a high elastic modulus and hardness, it is approximately 1.5 and 1.7 times as high as those of the coarse-grained region, respectively. The mean values of the elastic modulus and hardness of the interface zone between TiBw and fine-grained regions are both slightly higher than those of the fine- and coarse-grained regions. These phenomena indicate the presence of stress gradients in the dual-structure composites leading to prominent mechanical incompatibilities during deformation and producing HDI hardening effects.

Fig. 4*C* shows the true stress–strain curves for dual-structure Ti6Al4V-TiBw composites with different 3D-MPA spacings. The inset optical micrograph clearly shows well-defined dual structures with varying 3D-MPA spacings. The 3D-MPA spacings are 200, 125, 50, and 15 μm. As shown, the ductility increased with decreasing 3D-MPA spacing, reaching a maximum when the 3D-MPA spacing was approximately 15 μm. Interestingly, the YS did not increase as much as the UTS. Furthermore, the strain hardening capability increased with decreasing 3D-MPA spacing (*SI Appendix*, Fig. S7), indicating that decreasing the 3D-MPA spacing is more effective in enhancing the Θ value than YS. This finding suggested a significant impact of 3D-MPA spacing on the strain hardening capability of the dual structure. It can be inferred that there is very likely to be an optimal pellet size in the dual-structure Ti6Al4V-TiBw composites to achieve the best strength and ductility matching. Notably, some earlier studies on laminate structure also reported similar simultaneous improvements in the strength and ductility with changing interfacial spacing (44). In addition, optimizing the content proportion and distribution parameters of 3D-MPA are crucial for the strength-ductility synergy of the dual structure, and future studies could fruitfully explore this synergy by controlling the proportions of coarse and fine grains via preparing more refined spherical composite powder.

Microcrack Evolution and Failure. To understand the failure behavior of the dual-structure Ti6Al4V-TiBw composites, the evolution of microcracking was characterized by in situ tensile test via SEM, and the microstructures of the overall and primary structure are shown in Fig. 5 *A* and *B*, respectively. The results reveal that microcracks nucleate preferentially at TiBw in the hard region (the point marked by the golden arrow in Fig. 5*B*) during the early stage of plastic deformation (ε_T = 4.6%), just as in the homostructure Ti6Al4V-TiBw. As the strain further increases (ε_T = 9.2%), more microcracks are formed on TiBw, leading to sequential micro fragments. However, when the ensuing microcracks reach the interface between the TiBw and Ti6Al4V matrix, slip traces are observed in the fine-grained region around TiBw (golden line marked in Fig. 5*B*); this indicates that the Ti6Al4V matrix in the fine-grained region undergoes severe plastic deformation. In this deformation regime, these microcracks are strictly arrested. When the microcrack density in the 3D-MPA reaches a certain level, the microcracks in adjacent TiBw begin to coalesce by tearing the fine grains between them to form large microcracks (Fig. 5*C*). After the main crack enters the coarse-grained region, plastic deformation of the coarse-grained region can play a further role in blunting the main crack. Other evidence that the dual structure can either deflect or block crack propagation is shown in *SI Appendix*, Fig. S8; it shows the macroscopic fracture morphologies of dual-structure Ti6Al4V-TiBw composites in the direction parallel to loading axis. It can be seen that the crack is deflected on an extension route as it crosses the 3D-MPA. The morphology of the complex microcrack within the 3D-MPA is also presented in a perpendicular direction to loading axis. A large number of tear ribs or tough nests located around TiBw (*SI Appendix*, Fig. S9) indicate that the fine grains in the 3D-MPA effectively limit the development of early microcracks. This implies that our dual structure plays an influential toughening role in retarding crack extension and may display enhanced damage tolerance. This is the key to improve the elongation of the dual-structure composites. By observing the fracture surface (*SI Appendix*, Fig. S9), it is found that microcracks are distributed spatially in a uniform manner. The uniform crack distribution implies that the region far from the final fracture surface also experienced extensive deformation and deformation-induced damage. Such relatively homogeneous deformation and damage accumulation in the dual structure allows a concomitant enhancement of the energy of fracture, contributing to the overall toughness.

Here, the crack evolution from initiation, propagation to fracture failure is given for dual-structure Ti6Al4V-TiBw composites. The microcracks initiate on TiBw reinforcements at an early stage. With increasing applied load, microcracks gradually merge and form a main crack, and then, the main crack propagates to the coarse-grained region and can extend further, leading to the final failure of the composites. This development process is confirmed by the finite elemental simulation (Fig. 5*C*). Fig. 5*D* also shows the simulation of crack propagation from the fine-grained to the coarse-grained region. Here, a stretching model for a single circular fine-grained region in a coarse-grained matrix with a single pre-crack is considered. The comparison of crack evolution shows that the stress concentration zone in the dual structure is much smaller than that in the homostructure. Moreover, under the same total strain, the corresponding extended crack length of the homostructure is relatively longer, while the crack of the dual structure is still confined in the fine-grained region (Fig. 5*D*). This suggests that the heterogeneous grain structure provides good blunting ability against the main crack extension (45).

Fabrication Process of Dual-Structure Ti6Al4V-TiBw Composites. We proposed an innovative synthetic strategy for dual-structure Ti6Al4V-TiBw composites based on powder metallurgy (Fig. 6*A*). The strategy began with Ti-TiBw composite powder containing nano-TiBw as the raw material (33, 34). Based on the interdiffusion

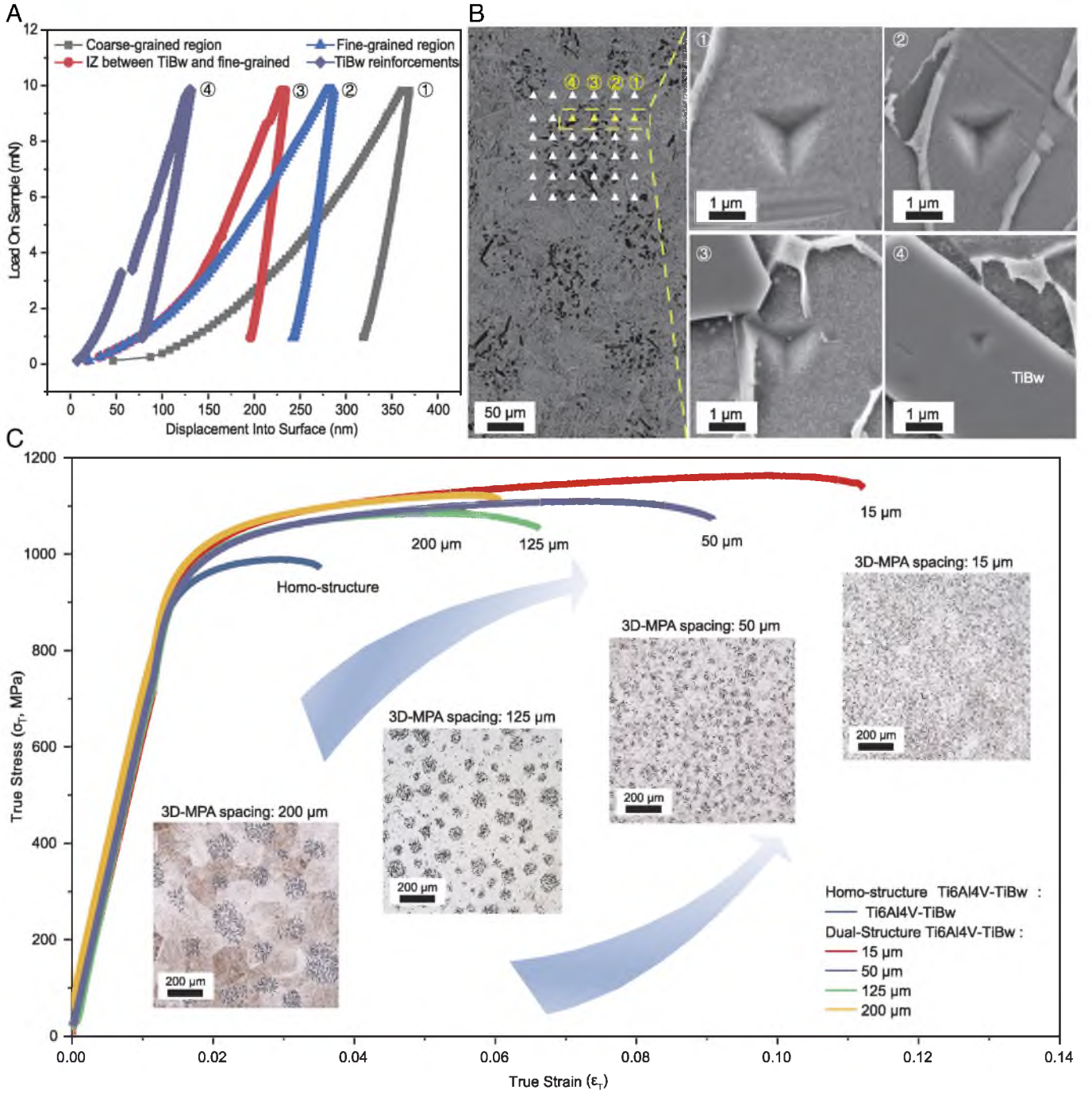

Fig. 4. The effect of the interface zone (IZ) between the TiBw and fine-grained region on the mechanical behaviors of the dual-structure Ti6Al4V-TiBw composites. (*A*) Nanoindentation load–displacement curves of the fine-grained region, coarse-grained region, TiBw reinforcements, and the IZ between TiBw and fine-grained region in dual-structure Ti6Al4V-TiBw composites. (*B*) Nanoindentation micrographs of the different regions. (*C*) True stress–strain curves vs. spacing of 3D-MPA, the given numbers reflect for the 3D-MPA spacing. The *Inset* shows the corresponding optical micrograph, where smaller spacing produces higher tensile strain.

reaction of Ti and Al components at high temperature according to the Ti-Al binary phase diagram (Fig. 6*B*), the alloying elements Al (6 wt.%) and V (4 wt.%) were elemental mixed with the Ti-TiBw composite powder to prepare powder mixture, which is consolidated by spark plasma sintering (SPS) to fabricate the dual-structure Ti6Al4V-TiBw composites (Fig. 6*B*). The fabrication process of our dual-structure composite can be divided into three steps (Fig. 6*A*). First, Ti-TiBw composite powder was prepared by EIGA, in which the fast cooling rate of the gas atomization process causes nano-TiBw to distribute along the GBs, similar to a quasi-continuous network structure (*SI Appendix*, Fig. S2). Second, the alloying elements Al and V were elemental premixed with Ti-TiBw composite powder to obtain a powder mixture. Finally, the dual-structure Ti6Al4V-TiBw composites comprising TiBw-rich region and TiBw-lean region were architected through the interdiffusion reaction between Ti and Al in the SPS sintering process by using the powder mixture, and the dual structure was obtained by sintering densification at 1,300 °C.

The success of this synthetic strategy relies on the self-organizational behavior of the TiBw-rich region induced by the interdiffusion reaction (46) between the alloying elements and the titanium matrix. Here, we prepared samples at different

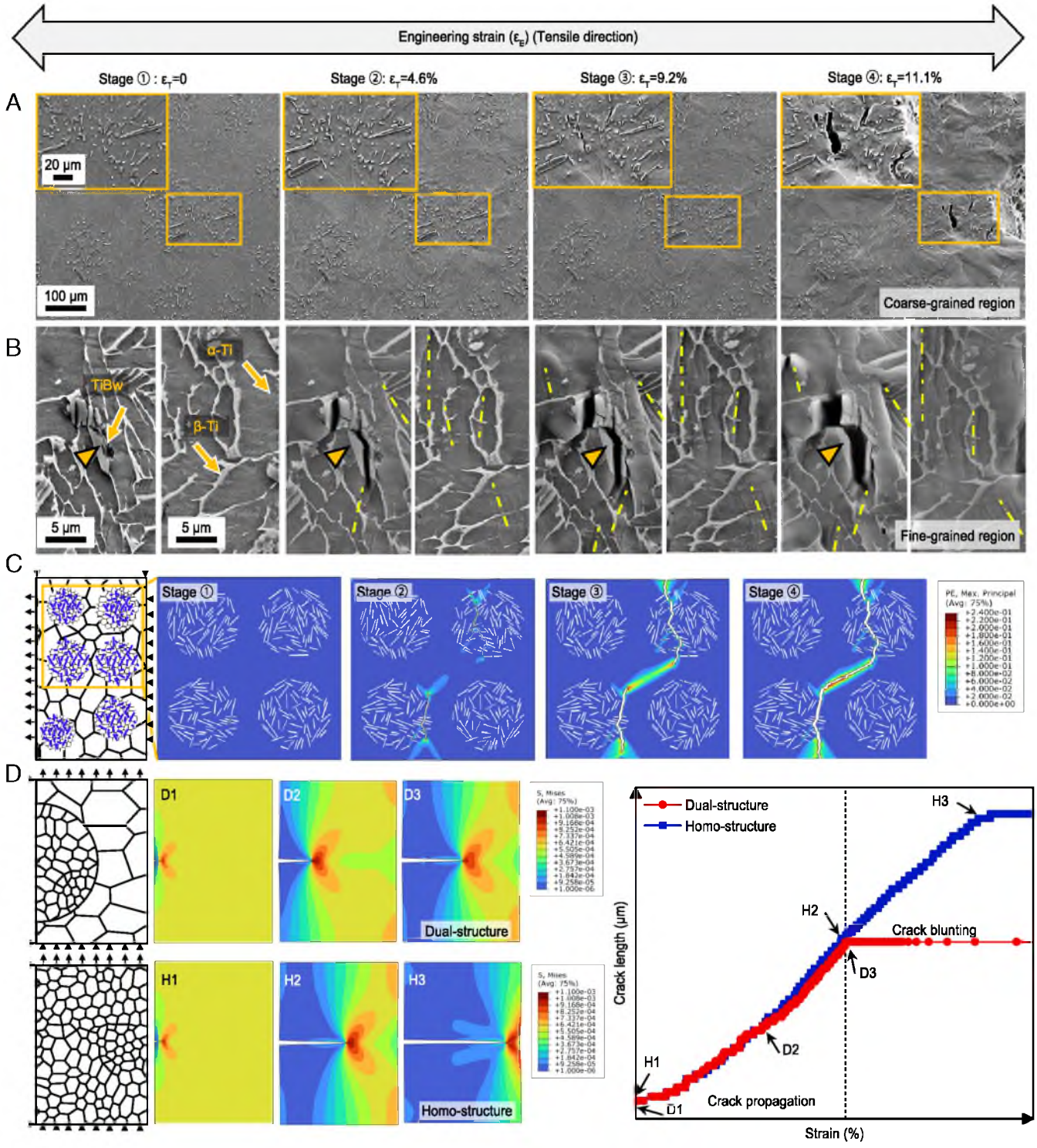

Fig. 5. Fracture and crack evolution of dual-structure Ti6Al4V-TiBw composites. (*A*) The snapshots of microcrack evolution in the coarse-grained region of the dual-structure under a strain in 0%, 4.6%, 9.2%, and 11.1%, respectively, and the local snapshot (*B*). (*C*) The numerical simulation for crack development process of crack evolution to failure in the dual-structure Ti6Al4V-TiBw composites. (*D*) The simulation of the crack propagation from the fine-grained region to the coarse-grained region. The model of dual structure includes material parameter settings for both fine- and coarse-grained regions, while the model of homostructure only has material settings for the fine-grained region. The hetero grain structure acts as a good blunting for the main crack extension.

sintering temperatures to unveil the formation process of the dual structure (*SI Appendix*, Supplementary Note 1). EPMA mapping results for the interdiffusion process between Ti and Al elements at different sintering temperatures are presented here (Fig. 6*C*). As shown in Fig. 6*C* ①, near the Al melting point (~660 °C), the Al layer is formed at the interface of the spherical Ti-TiBw composite powder and gradually transforms into the $TiAl_3$ layer. As the sintering temperature is further increased to 850 °C, due to the concentration gradient between Al and Ti, Ti elements in the Ti layer and Al elements in the $TiAl_3$ layer undergo interdiffusion reactions to form $TiAl_2$, TiAl, and Ti_3Al layers, as shown in Fig. 6*C* ②. When continuing to increase the temperature to 1,000 °C, Ti and Al interdiffusion occurs continuously, and the thickness of the $TiAl_3$ layer gradually decreases,

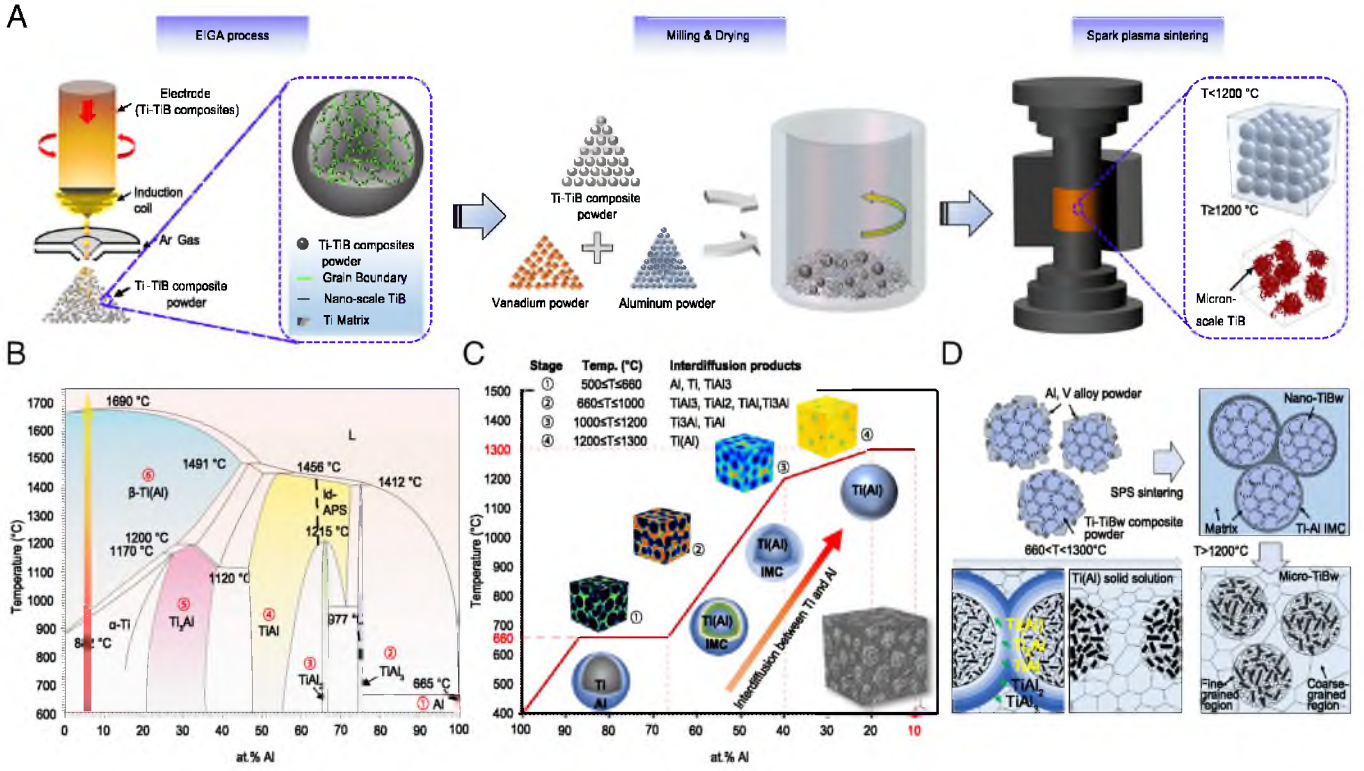

Fig. 6. Schematic diagram of fabrication processes and design concept of dual-structure Ti6Al4V-TiBw composites via interdiffusion self-organization strategy. (*A*) Fabrication process of dual-structure Ti6Al4V-TiBw composites. (*B*) The reaction routes of stepwise formation of Ti-Al intermetallic compounds on Ti-Al binary phase diagrams. (*C*) The electron probe microanalysis (EPMA) of the elemental interdiffusion process and the formation of dual-structure Ti6Al4V-TiBw composites. (*D*) Schematic diagram of the formation of dual-structure Ti6Al4V-TiBw composites and the Ti-Al interdiffusion process.

while $TiAl_2$, TiAl, and Ti_3Al phases compete for growth until $TiAl_3$ and $TiAl_2$ layers are depleted, and finally, Ti_3Al/TiAl layers are obtained (Fig. 6*C*③. As the sintering temperature continues to increase, interdiffusion between Ti and Al in the Ti_3Al/TiAl layer continues until the Ti (Al) solid solution is formed (T > 1,200 °C, where the maximum solid solution of Al in Ti is elevated to ~30 at.%) (47), as shown in Fig. 5*C*④. This coincides with the results of XRD analyses at different sintering temperatures (*SI Appendix*, Fig. S10). In addition, the EPMA point scan results (*SI Appendix*, Fig. S11) also further demonstrate the interdiffusion reaction process and the decomposition of its product, where the results are highly consistent with the Ti-Al binary phase diagram. Notably, Fig. 6*D* and *SI Appendix* (*SI Appendix*, Fig. S12) demonstrate that the interdiffusion reaction between the alloying element Al and the matrix Ti induces the self-organizational behavior of TiBw, which directly creates the 3D-MPA architecture of the dual-structure composite.

Our interdiffusion-based powder metallurgy strategy paves a way for developing dual-structure TMCs. For other metal systems, alloying elements are required to meet the following criteria: i) a certain solubility in the matrix, ii) low melting point, iii) interdiffusion with the matrix element, and iv) no chemical reaction with the reinforcements. Following these criteria, it is possible to prepare dual-structure composites through our interdiffusion-based powder metallurgy strategy. Aluminum, copper, steel, and titanium alloys and their matrix composites are all expected to form a dual structure, e.g., Cu(Zn/Sn/Al)-TiB_2/Al_2O_3/SiC and Ti(Al-V)-TiC. Therefore, our interdiffusion-based powder metallurgy strategy can be extended to other MMC systems to promote the development of good strength-ductility synergy. This also raises the possibility of improving trade-offs in other properties (e.g., magnetization strength-coercivity, conductivity and Seebeck coefficient, and ferromagnetism and ferroelectricity) for some functional materials (29, 48).

In summary, we have demonstrated a dual-structure Ti6Al4V-TiBw composite that achieves good strength and loss-free ductility. It is known that the dual structure generates a heterogeneous grain structure in the matrix and that the interactions between heterogeneous grain regions give the reinforcements a high deformation capacity, which enables deformation coordination in dual-structure composites. In addition, the HDI hardening effect further enhances the strain hardening ability of the composites. As a result, the developed dual-structure Ti6Al4V-TiBw composites exhibits an ideal ductility which is comparable to that of Ti6Al4V alloys. This dual structure and its fabrication strategy provide an enlightening way to solve the strength-ductility trade-off of TMCs and can also be applied to high-performance and functional designs of other metallic materials and MMCs.

Materials and Methods

Preparation of Dual-Structure Ti6Al4V-TiBw Composites. First, 98 wt.% titanium sponge powder with a purity of 99.9% and 2 wt.% TiB_2 powder (d = 1 to 3 μm) with a purity of 99.9% were used as raw materials, which were provided by Avimetal Powder Metallurgy Technology Co., Ltd., China. Ti-TiBw composites were fabricated via vacuum arc remelting according to the in situ reaction $Ti+TiB_2 \rightarrow 2TiB$ to homogeneously distribute the TiB reinforcements in the ingot. Then, the Ti-TiBw composite powder was produced by EIGA. Based on this, spherical Ti-TiBw composite powder and commercially available Al powder (purity of 99.85%, 6 wt.%) with particle sizes of ~20 μm and V powder (purity of 99.85%, 4 wt.%) with an average particle size of 10 μm were pre-mixed by low-energy ball milling with rotation at 250 rpm and a mixing time of 4 h. Finally, the as-milled powder mixtures were sintered by SPS technology at 1,300 °C and under a pressure of 30 MPa for 30 min to obtain dual-structure Ti6Al4V-TiBw composites.

Microstructural Characterization. The microstructures of the Ti-TiBw composite powder, bulk sample, and fracture surfaces of the samples were characterized using scanning electron microscopy (SEM, JSM-6700F, JEOL, Japan), electron backscattered diffraction (EBSD), and transmission electron microscopy (TEM, JEM-2010, JEOL, Japan). The in situ EBSD experiments were conducted using a field emission scanning electron microscope (FE-SEM, JSM-6500F) equipped with an EBSD detector, and the microstructure on the normal plane was characterized by EBSD using a step of 0.4 μm. The synchrotron radiation imaging experiments were performed at the 3W1E beamline of the Beijing Synchrotron Radiation Facility (BSRF). Micropillars with diameters of ~1 mm for mounting were prepared by electrical discharge machining and subsequent mechanical polishing. Imaging was conducted using a 55 keV monochromatic X-ray beam. X-ray diffraction (XRD, XRD-7000, SHIMADZU, Japan) was employed to confirm the phase compositions of the sintered samples. Electron probe microanalysis (EPMA, JXA-8530F, Japan) was mainly used to observe the element distributions of the sintered samples made at different sintering temperatures, while the backscattered electron (BSE) SEM imaging mode was used to identify the microstructures of the composites.

Mechanical Property Measurements. This work involved three kinds of tensile tests. To observe the deformation behavior and damage evolution of the dual-structure Ti6Al4V-TiBw composites in real time, in situ tensile tests were performed on an additional tensile device equipped with a Quanta FEG-450 SEM microscope operating at a tensile speed of 1 $\mu m\ s^{-1}$. In situ tensile tests were performed by using 0.7 mm thick dog-bone-shaped samples with a gauge length of 1.5 mm and a gauge width of 1.5 mm, which were machined with electrical discharge machining. Both faces of the samples were ground with 2,000 grade SiC paper. One face was then polished using a nanosilica slurry and etched using Kroll reagent for 10 s. To analyze the fracture mode from the fracture morphology and test the hetero-deformation-induced (HDI) stress, the sintered samples were cut to a gauge dimension with a diameter of 3 mm and a length of 15 mm. Both uniaxial tensile tests and loading–unloading–reloading (LUR) tensile tests were carried out with a universal tensile machine (AGS-X, ZhongJi, China) operating at a strain rate of $5 \times 10^{-4}\ S^{-1}$ at room temperature, and each test was repeated for at least three samples to ensure data reproducibility. An extensometer was used to measure the strain during the tensile test. The test was conducted according to the Oliver & Pharr approach by means of quasistatic nanoindentation technology, the maximum load was set to 10 mN, and the loading rate was 0.5 nm/s. The hardness distribution of the fine-grained region, coarse-grained region, TiBw reinforcements, and interface zone between TiBw and fine-grained region in the dual-structure Ti6Al4V-TiBw composites were determined by nanoindentation tests using a Nano-Indenter G200 machine. Nanoindents were applied in a 6 × 6 array (36 indentations) in the sample with a spacing of 40 μm on the 3D-MPA to a maximum load of 10 mN, and the loading rate was 0.1 nm/s.

Simulations

Tensile Simulation of Samples Embedded with Four Randomly Reinforced Pellets. To explore the behavior characteristics of the whiskers and fine- and coarse-grained regions in the fracture process, we performed a 2D model simulation of tensile fracture by using ABAQUS software. Both the length and width of the samples were set to 600 μm. Four circular fine-grained regions with diameters of 240 μm were symmetrically placed in the center of the four symmetrical segmented blocks of each sample. The reinforcing TiBw was randomly filled in the four circular fine-grained regions, and the ratio of the total area of the whiskers to the circular area of the fine-grained region was approximately 8%. In the simulation of the tensile process, the brittle fracture model was used to describe the brittle fracture behavior of TiBw, and the ductile damage model was employed to describe the tensile failure behavior of the matrix with fine grains and coarse grains. Specifically, for TiBw, the type of brittle cracking was set as strain, the direct stress after cracking was (0.85, 0) with units of GPa, and the corresponding direct cracking strain was (0, 0.05). The shear retention model uses the power law form, $\rho(\bar{e}^{ck}_{nn}) = (1-\bar{e}^{ck}_{nn}/\bar{e}^{ck}_{max})^{p}$, where ρ and $\bar{e}^{ck}_{max}$ are material parameters (here, $p = 1$, and $\bar{e}^{ck}_{max} = 0.05$). For matrices with fine and coarse grains, an empirical phenomenological model for predicting the onset of damage of Ti6Al4V alloys was employed. For the ductile damage model of bulk Ti6Al4V, the displacement type of damage evolution is linear, the fracture strain is 0.1, stress triaxiality is 0.33, and the displacement at failure is 0.05 μm. The plastic constitutive equation of Ti6Al4V is $\sigma = A + K(\varepsilon^{p})^{n}$, where A, K, ε^{p} and n denote the initial yield stress, strain hardening coefficient, plastic strain, and hardening exponent, respectively. According to Hall–Petch theory (49, 50), the correlation between yield strength and grain size can be expressed as $\sigma_y = \sigma_0 + k_y D^{-1/2}$, where σ_y is the yield stress, σ_0 is the back stress due to lattice friction, k_y is the Hall–Petch coefficient, and D is the average diameter of the grains. For Ti6Al4V, the fitting parameters of the Hall–Petch relationship were obtained from the best fit of the experimental data (49). The yield stress values (772 MPa for the sample with coarse grains, 833 MPa for the sample with fine grains) related to the grain size were obtained by directly substituting the average grain diameters ($d_{coarse} = 42.3\ \mu m$, $d_{fine} = 5.8\ \mu m$) in the fine- and coarse-grained regions measured in the experiment into the formula. Please refer to *SI Appendix*, Supplementary Note 3 for detailed model theory and relevant material parameters.

Passivation Effect of the Dual Structure on Crack Propagation. To deeply understand the influence of heterostructures on crack passivation behavior, crack propagation analysis was performed by using extended finite element method (XFEM)-based cohesive segments with linear elastic traction-separation behavior. We considered two comparative simulation examples: 1) the crack propagation simulation of a homogeneous material, whose cross-sectional parameters are the linear elastic crack propagation mechanical parameters and the simulation box size is 150 μm × 200 μm, and 2) a heterogeneous simulation model composed of a fine-grained crack growth region and a coarse-grained ductile damage region, with the same simulation size of 150 μm × 200 μm. The fine-grained region is a semicircular area with a radius of 80 μm whose center is at the midpoint of the line on the left side of the box. The fine-grained region is the cross-sectional parameter of linear elastic crack growth, and the coarse grain area is the ductile damage model. The failure mechanism consists of two parts: a damage initiation criterion and a damage evolution law. During sample loading, the crack length of an existing crack is extended after an equilibrium increment when the fracture criterion, $1.0 \le f \le 1.0 + f_{tol}$, reaches the value of one within a given tolerance $f_{tol} = 0.05$. The damage evolution law describes the rate at which the cohesive stiffness is degraded once the corresponding initiation criterion is reached. In our simulation, the maximum principal stress is 1.1 GPa, and the fracture energy is 5.5 Pa m, which results in a complete separation crack spacing of 10 μm. Please refer to *SI Appendix*, Supplementary Note 3 for detailed model theory and relevant material parameters.

Data, Materials, and Software Availability. All study data are included in the article and/or supporting information.

ACKNOWLEDGMENTS. This work was supported by the National Key R&D Program of China (Grant No. 2021YFB3701203), the National Natural Science Foundation of China (Grant No. 52201165), Shaanxi Innovative Research Team for Key Science and Technology (Grant No. 2023-CX-TD-46), Xi'an University of Technology Doctoral Dissertation Innovation Fund (Grant No. 310-252072101), and Doctoral Teacher Starting Fund of Xi'an University of Technology (Grant No. 101-451121007).

Author affiliations: [a]School of Materials Science and Engineering, Xi'an University of Technology, Xi'an, Shaanxi 710048, China; [b]Xi'an Key Laboratory of Advanced Powder Metallurgy Materials and New Technology, Xi'an, Shaanxi 710048, China; [c]Xi'an Sailong Additive Technology Co., Ltd., Xi'an 710018, China; [d]School of Civil Engineering, Xi'an University of Architecture and Technology, Xi'an, Shaanxi 710055, China; [e]School of Mathematics and Statistics, Ningxia University, Yinchuan, Ningxia 750021, China; [f]Joining and Welding Research Institute, Osaka University, Ibaraki, Osaka 567-0047, Japan; [g]Razak Faculty of Technology and Informatics, Universiti Teknologi Malaysia, Jalan Sultan Yahya Petra, Kuala Lumpur 54100, Malaysia; [h]Institute of High Energy Physics, Chinese Academy of Sciences, Beijing 100049, China; and [i]Centre of Excellence for Advanced Materials, Guangdong, Dongguan 523808, China

1. D. Raabe, C. C. Tasan, E. A. Olivetti, Strategies for improving the sustainability of structural metals. *Nature* **575**, 64–74 (2019).
2. K. Lu, The future of metals. *Science* **328**, 319–320 (2010).
3. R. O. Ritchie, The conflicts between strength and toughness. *Nat. Mater.* **10**, 817–822 (2011).
4. G. Singh, U. Ramamurty, Boron modified titanium alloys. *Prog. Mater. Sci.* **111**, 100653 (2020).
5. S. H. Jiang *et al.*, Ultrastrong steel via minimal lattice misfit and high-density nanoprecipitation. *Nature* **544**, 460–464 (2017).
6. T. Gladman, Precipitation hardening in metals. *Mater Sci. Technol.* **15**, 30–36 (1999).
7. S. Tang *et al.*, Precipitation strengthening in an ultralight magnesium alloy. *Nat. Commun.* **10**, 1003 (2019).
8. Z. Li *et al.*, A nanodispersion-in-nanograins strategy for ultra-strong, ductile and stable metal nanocomposites. *Nat. Commun.* **13**, 5581 (2022).
9. J. H. Gao *et al.*, Facile route to bulk ultrafine-grain steels for high strength and ductility. *Nature* **590**, 262–267 (2021).
10. G. Liu *et al.*, Nanostructured high-strength molybdenum alloys with unprecedented tensile ductility. *Nat. Mater.* **12**, 344–350 (2013).
11. H. Wu, G. H. Fan, An overview of tailoring strain delocalization for strength-ductility synergy. *Prog. Mater. Sci.* **113**, 100675 (2020).
12. D. Lunt, T. Busolo, X. Xu, J. Q. D. Fonseca, M. Preuss, Effect of nanoscale α_2 precipitation on strain localisation in a two-phase Ti-alloy. *Acta Mater.* **129**, 72–82 (2017).
13. D. Lunt, X. Xu, T. Busolo, J. Q. D. Fonseca, M. Preuss, Quantification of strain localisation in a bimodal two-phase titanium alloy. *Scr. Mater.* **145**, 45–49 (2018).
14. K. Lu, L. Lu, S. Suresh, Strengthening materials by engineering coherent internal boundaries at the nanoscale. *Science* **324**, 349–352 (2009).
15. J. Y. He *et al.*, A precipitation-hardened high-entropy alloy with outstanding tensile properties. *Acta Mater.* **102**, 187–196 (2016).
16. X. D. Rong *et al.*, Revealing the strengthening and toughening mechanisms of Al-CuO composite fabricated via in-situ solid-state reaction. *Acta Mater.* **204**, 116524 (2021).
17. Z. Dong, Z. Q. Ma, L. M. Yu, Y. C. Liu, Achieving high strength and ductility in ODS-W alloy by employing oxide@W core-shell nanopowder as precursor. *Nat. Commun.* **12**, 5052 (2021).
18. G. L. Fan, Z. Q. Guo, Z. Q. Tan, Z. Q. Li, Architecture design strategies and strengthening-toughening mechanisms of metal matrix composites. *Acta Metall. Sin.* **58**, 1416–1426 (2022).
19. A. Mortensen, J. Llorca, Metal matrix composites. *Annu. Rev. Mater. Res.* **40**, 243–270 (2010).
20. U. G. K. Wegst, H. Bai, E. Saiz, A. P. Tomsia, R. O. Ritchie, Bioinspired structural materials. *Nat. Mater.* **14**, 23–26 (2015).
21. L. J. Huang, L. Geng, H. X. Peng, Microstructurally inhomogeneous composites: Is a homogeneous reinforcement distribution optimal? *Prog. Mater. Sci.* **71**, 93–168 (2015).
22. L. J. Huang *et al.*, Multiscale architecture and superior high-temperature performance of discontinuously reinforced titanium matrix composites. *Adv. Mater* **33**, 2000688 (2021).
23. X. Luo *et al.*, Evading strength and ductility trade-off in an inverse nacre structured magnesium matrix nanocomposite. *Acta Mater.* **228**, 117730 (2022).
24. Z. Li *et al.*, Enhanced mechanical properties of graphene (reduced graphene oxide)/aluminum composites with a bioinspired nanolaminated structure. *Nano Lett.* **15**, 8077–8083 (2015).
25. X. W. Fu *et al.*, Trimodal grain structure enables high-strength CNT/Al-Cu-Mg composites higher ductility by powder assembly & alloying. *Mater. Res. Lett.* **9**, 50–57 (2021).
26. R. J. Moon, M. Tilbrook, M. Hoffman, A. Neubrand, Al-Al_2O_3 composites with interpenetrating network structures: Composite modulus estimation. *J. Am. Ceram. Soc.* **88**, 666–674 (2005).
27. X. Zhang *et al.*, A powder-metallurgy-based strategy toward threedimensional graphene-like network for reinforcing copper matrix composites. *Nat. Commun.* **11**, 2775 (2020).
28. H. J. Gao, Y. Huang, W. D. Nix, Mechanism-based strain gradient plasticity–I. Theory. *J. Mech. Phys. Solids* **47**, 1239–1263 (1999).
29. Y. T. Zhu, X. L. Wu, Heterostructured materials. *Prog. Mater Sci.* **131**, 101019 (2023).
30. L. J. Huang, L. Geng, H. X. Peng, J. Zhang, Room temperature tensile fracture characteristics of in situ TiBw/Ti6Al4V composites with a quasi-continuous network architecture. *Scr. Mater* **64**, 844–847 (2011).
31. T. M. T. Godfrey, A. Wisbey, P. S. Goodwin, K. Bagnall, C. M. Ward-Close, Microstructure and tensile properties of mechanically alloyed Ti-6Al-4V with boron additions. *Mater. Sci. Eng. A* **282**, 240–250 (2000).
32. L. J. Huang, L. Geng, H. X. Peng, In situ (TiBw + TiCp)/Ti6Al4V composites with a network reinforcement distribution *Mater. Sci. Eng. A* **527**, 6723–6727 (2010).
33. D. Pan *et al.*, Enhanced strength and ductility of nano-TiBw-reinforced titanium matrix composites fabricated by electron beam powder bed fusion using Ti6Al4V-TiBw composite powder. *Addit. Manuf.* **50**, 102519 (2022).
34. D. Pan *et al.*, TiB nano-whiskers reinforced titanium matrix composites with novel nano-reticulated microstructure and high performance via composite powder by selective laser melting. *Mater. Sci. Eng. A* **799**, 140137 (2021).
35. S. Lakra, T. K. Bandyopadhyay, S. Das, K. Das, Synthesis and characterization of in-situ (Al-Al_3Ti-Al_2O_3)/Al dual matrix composite. *J. Alloy Compd.* **842**, 155745 (2020).
36. L. Jiang *et al.*, Toughening of aluminum matrix nanocomposites via spatial arrays of boron carbide spherical nanoparticles. *Acta Mater.* **103**, 128–140 (2016).
37. Y. T. Zhu *et al.*, Heterostructured materials: Superior properties from hetero-zone interaction. *Mater Res. Lett.* **9**, 1–31 (2021).
38. P. J. Shi *et al.*, Enhanced strength-ductility synergy in ultrafine-grained eutectic high-entropy alloys by inheriting microstructural lamellae. *Nat. Commun.* **10**, 489 (2019).
39. M. Calcagnotto, D. Ponge, E. Demir, D. Raabe, Orientation gradients and geometrically necessary dislocations in ultrafine grained dual-phase steels studied by 2D and 3D EBSD. *Mater. Sci. Eng. A* **527**, 2738–2746 (2010).
40. M. F. Ashby, The deformation of plastically non-homogeneous materials. *Philos. Magazine* **21**, 399–424 (1970).
41. J. Jiang, T. B. Britton, A. J. Wilkinson, Evolution of dislocation density distributions in copper during tensile deformation. *Acta Mater.* **61**, 7227–7239 (2013).
42. K. Lin, P. S. Dai, The influence of thermal residual stresses and thermal generated dislocation on the mechanical response of particulate-reinforced metal matrix nanocomposites. *Compos. B. Eng.* **83**, 105–116 (2015).
43. N. Hansen, Hall-Petch relation and boundary strengthening. *Scr. Mater* **51**, 801–806 (2004).
44. X. L. Ma *et al.*, Mechanical properties of copper/bronze laminates: Role of interfaces. *Acta Mater.* **116**, 43–52 (2016).
45. Z. Y. Liu *et al.*, Enhancement of the strength-ductility relationship for carbon nanotube/Al-Cu-Mg nanocomposites by material parameter optimization. *Carbon* **157**, 602–613 (2020).
46. Y. Mishin, C. Herzig, Diffusion in the Ti–Al system. *Acta Mater.* **48**, 589–623 (2000).
47. X. P. Cui *et al.*, Fabrication of fully dense TiAl-based composite sheets with a novel microlaminated microstructure. *Scr. Mater.* **66**, 276–279 (2012).
48. L. Lou *et al.*, Directional magnetization reversal enables ultrahigh energy density in gradient nanostructures. *Adv. Mater.* **33**, 2102800 (2021).
49. Y. Chong *et al.*, Yielding nature and Hall-Petch relationships in Ti-6Al-4V alloy with fully equiaxed and bimodal microstructures. *Scr. Mater.* **172**, 77–82 (2019).
50. M. T. Jia, D. L. Zhang, B. Gabbitas, J. M. Liang, C. Kong, A novel Ti-6Al-4V alloy microstructure with very high strength and good ductility. *Scr. Mater.* **107**, 10–13 (2015).